

Chapter 1

Planetesimal/Debris discs

Sebastian Marino

Jesus College, University of Cambridge

Jesus Lane, Cambridge, CB5 8BL, UK

sebastian.marino.estay@gmail.com

This review chapter for young researchers presents our current understanding of debris discs. It introduces some of their basic properties and observables, and describes how we think they form and collisionally evolve. Special emphasis is dedicated to ALMA observations of the dust and gas, which constrains the distribution of planetesimals, their volatile composition, and potential volatile delivery to planetary atmospheres.

1. What are debris discs?

As usual, establishing an astrophysical definition for a broad phenomenon that sometimes overlays with other types of circumstellar discs is challenging. Hence, it is perhaps clearer to answer this from a Solar System perspective. The Solar System's debris disc is made of all its non-planetary components. Namely, the Asteroid belt, the Kuiper belt, the Oort cloud, the Zodiacal cloud, Jupiter family comets, etc. These are a natural part of planetary systems, and today we know of hundreds of extrasolar analogues.

The study of the Solar System's debris disc has been fundamental for the development of planetary dynamics and elucidating the and history of the Solar System planets. Similarly, studying debris discs around other stars is crucial for obtaining a holistic view of planetary systems. Most debris discs are discovered thanks to the infrared (IR) excess emitted by circumstellar dust, first detected around a few nearby stars almost four decades ago (Aumann et al., 1984). The fact that dust is short-lived against collisions and radiation forces compared to the ages of these systems (Backman & Paresce, 1993), means that the observed dust is continuously replenished by collisions of longer-lived bodies such as km-sized asteroids or comets. Since

then, multiwavelength studies have shown that these dusty discs are a ubiquitous component of planetary systems, they also possess a gas component, and our Solar System's debris disc might not be the norm. Dust and gas observations allow us to study this non-planetary component and constrain their composition, evolution and dynamics.

This chapter aims to serve as an introduction to debris discs and summarise the latest advances in this field, making a special emphasis in what we have learnt from observations of gas and dust with the Atacama Large Millimeter/submillimeter Array (ALMA) in the last 3 years. Previous reviews by Wyatt (2008), Krivov (2010), Matthews et al. (2014) and Hughes et al. (2018) cover at great length the initial discovery of debris discs around other stars since the launch of the Infrared Astronomical Satellite (IRAS), their basic observables, detection limits, their expected evolution, the diversity of disc structures, dust properties, and variability, and thus are excellent references for eager readers. One important class of debris discs that is not covered here is the discs around polluted white dwarfs, which has been recently covered in detail by Veras (2021).

2. Basic properties and observables

The solid component of debris discs is made of solids with a wide size distribution, ranging from μm -sized dust up to km-sized or even larger planetesimals. This distribution is regulated by collisions that grind down solids moving mass from large to small bodies, and the removal of small dust by radiation pressure and Poynting-Robertson (P-R) drag (e.g. Löhne et al., 2008). Since the expected size (a) distribution is close to $dN \propto a^{-3.5} da$, the bulk of the cross sectional area is dominated by the smallest grains at the bottom of the size distribution, while the mass is dominated by the largest bodies. This means that debris disc observations trace the smallest debris that are constantly destroyed and replenished in this collisional cascade.

Two fundamental properties of debris discs can be obtained from unresolved observations that constrain their spectral energy distribution (SED). First, we can derive the blackbody temperature of the emission using Wien displacement law. Then, assuming dust behaves approximately like blackbodies, this temperature (T_{BB}) and the known stellar luminosity (L_{\star}) can be used to infer the characteristic radius of the disc, sometimes called blackbody radius r_{BB} ,

$$r_{\text{BB}} = 1 \text{ au} \left(\frac{278.3 \text{ K}}{T_{\text{BB}}} \right)^2 \left(\frac{L_{\star}}{L_{\odot}} \right)^{0.5}. \quad (1)$$

Note that r_{BB} is usually smaller than the true radius (r_{belt}) due to small grains being inefficient emitters at IR wavelengths, hence having higher equilibrium temperatures than blackbodies (Booth et al., 2013; Kennedy & Wyatt, 2014; Pawellek et al., 2014). Some systems can also display more than one temperature, typically with a peak of emission at far-IR wavelengths and significant emission in the mid-IR. Figure 1 shows an example of such a system with two temperature components. Such systems are inferred to have a cold Kuiper belt analogue at tens of au, i.e. an *exoKuiper belt*, and a warm component analogous to the Asteroid belt or Zodiacal cloud closer in (e.g. Backman et al., 2009; Chen et al., 2009; Morales et al., 2009; Ballering et al., 2014; Kennedy & Wyatt, 2014).

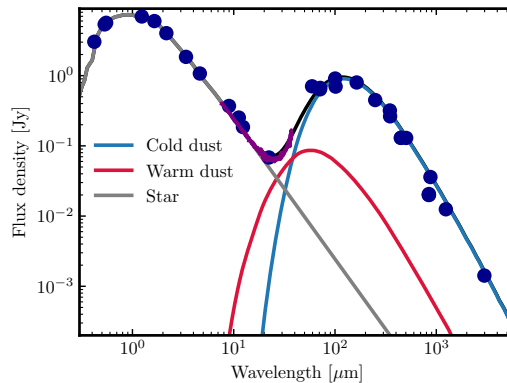


Fig. 1. Spectral energy distribution of HD 107146. The blue points and purple line represent photometric measurements and an Spitzer/IRS spectrum, respectively. The solid lines represent the emission from the star (grey) and two dust components with different temperatures (adapted from Marino et al. 2018a).

The second most important property is the disc fractional luminosity (f_{IR}), defined as the ratio between the dust and stellar luminosities. Since debris discs are optically thin, f_{IR} is approximately $\sigma_{\text{tot}}/(4\pi r_{\text{belt}}^2)$, where σ_{tot} is the total absorption cross-sectional area of the dust. Therefore, the SED provides direct constraints to the amount of dust in a system.

There are additional constraints that can be derived from SEDs. For example, the spectral slope of the dust emission depends on the dust opacity, which depends on the size distribution. Thus, it is in principle possible to constraint the size distribution and test collisional models (Ricci et al., 2015; MacGregor et al., 2016). However, uncertainties about the compo-

sition and structure of grains means that size distribution measurements suffer from great systematic uncertainties (Löhne, 2020).

Far-IR surveys with *Spitzer* and *Herschel* have characterised the frequency of cold debris discs around nearby stars with fractional luminosities $\gtrsim 10^{-6}$, obtaining detection rates of 30% around A stars (Su et al., 2006) and about 20% for FGK stars (Eiroa et al., 2013; Sibthorpe et al., 2018). Note that these percentages are not occurrences, but rather detection rates above a given sensitivity limit. As a reference, the Kuiper belt would be more than an order of magnitude below the detectability threshold of such surveys, and thus it is possible that every star has a debris disc at least as massive as the Kuiper belt. This sensitivity limit is specially poor for surveys around M stars, which have yielded detection rates of only 2-14% as these discs tend to be colder and thus harder to detect in the far-IR (Kennedy et al., 2018; Luppe et al., 2020). Moreover, the detection rates are also sensitive to the age of the sample considered. Pawellek et al. (2021) showed how debris discs are found around $\sim 75\%$ of F stars in the 23 Myr old β Pic Moving Group. This suggests that the real incidence of massive debris discs could be much higher, and heavily dependent on the age.

Recent studies have also searched for correlations between the presence of planets and debris discs. Meshkat et al. (2017) looked at $5 - 20 M_{\text{Jup}}$ planets at separations $10 - 1000$ au, detected through direct imaging, and found tentative evidence of a higher occurrence rate of planets in systems with detected debris discs. Therefore, it appears that the formation of massive exoKuiper belts is favoured in systems that also form gas giants at wide separations. On the other hand, Yelverton et al. (2020) found no significant difference in the fractional luminosity or temperature distributions of debris discs around stars with and without close-in planets detected through radial velocities. Finally, it is worth noting that debris discs detection rates seems to be unaffected by the presence of binaries at separations greater than 135 au, halved by the presence of binaries at separations smaller than 25 au, and reduces to zero for binaries with intermediate separation that roughly overlay with typical debris disc sizes (Yelverton et al., 2019).

2.1. Debris disc formation

The existence of debris discs requires the formation of planetesimals in protoplanetary discs. These km-sized bodies must grow from the dust in protoplanetary discs. However, their formation encounters multiple barriers that prevent dust from growing beyond cm sizes due to their radial drift (Whip-

ple, 1973; Weidenschilling, 1977), or bouncing and fragmentation (Zsom et al., 2010; Blum & Wurm, 2008). The first barrier can be circumvented by a pressure maxima in the gas, which act as traps where dust can survive, accumulate and efficiently grow to cm sizes. Strong evidence of such dust traps is seen in the axisymmetric rings (Dullemond et al., 2018; Rosotti et al., 2020) and clumps in protoplanetary discs (Casassus et al., 2019).

Two mechanisms have been proposed to overcome the second barrier. First, dust grains could grow as very porous fractals that remain sticky and well coupled to the gas, bypassing both the radial drift and fragmentation/bouncing barrier (Kataoka et al., 2013). This relies, however, on the assumption of a high stickiness which is still uncertain. A second and perhaps more robust scenario is the streaming instability (Youdin & Goodman, 2005; Johansen et al., 2007). This instability is triggered when the dust densities reach values similar to the gas densities, and dust is large enough to be slightly decoupled from the gas (see Li & Youdin, 2021). This instability results in the collapse of dust clouds and the formation of ~ 100 km-sized planetesimals. It has been shown that dust growth, their settling to the midplane and concentration in radial or azimuthal dust traps (as the ones observed) is enough to trigger the streaming instability (Stammler et al., 2019; Carrera et al., 2021). The newborn planetesimals might continue growing via mutual collisions, but never reach a mass high enough to clear their orbits. This is the last condition for debris disc formation, which is not problematic given the extremely long growth timescales of planetesimals at tens of au (e.g. Kenyon & Bromley, 2008).

To constrain debris disc formation further, recent ALMA surveys have looked at class III stars, i.e. those that have recently lost their protoplanetary discs, to look for the youngest debris discs and compare them with the older populations (Lovell et al., 2021a; Michel et al., 2021). For example, the debris disc detection rate in class III stars in Lupus is consistent with population models that fit older stars, suggesting that debris disc formation does not require long-lived protoplanetary discs (Lovell et al., 2021a).

3. Collisional evolution

After the dispersal of protoplanetary discs, planetesimals orbits can be stirred, for example, through secular interactions with planets (Mustill & Wyatt, 2009), or through close encounters with massive planetesimals in the disc (Kenyon & Bromley, 2008; Krivov & Booth, 2018). Stirring results in orbit crossing and relative velocities that are high enough to fragment

km-sized planetesimals and trigger a collisional cascade that resupplies the observed dust. The collisional evolution has been studied in detail both analytically (e.g. Dominik & Decin, 2003; Wyatt et al., 2007b; Löhne et al., 2008), and using numerical simulations (Krivov et al., 2006; Thébault & Augereau, 2007; Gáspár et al., 2012). Here I summarise some simple equations that can be used to estimate the collisional timescales of debris discs.

First, let's consider a size distribution of the form $dN = D^{2-3q}dD$, where D is the diameter of solids and $-q$ is the power-law index of the mass distribution ($dN = m^{-q}dm$). Generally speaking, for q in the range between $5/3$ and 2 , we have that most of the disc mass is in the objects close to the maximum size D_{\max} and the surface area is dominated by solids close to the minimum size D_{\min} . In debris discs, away from the edges of the size distribution, we typically expect q to take values close to $11/6$ ($dN = D^{-3.5}dD$). This value is only truly valid for an infinite collisional cascade where the strength of solids is independent of size (Dohnanyi, 1969). Nevertheless, the estimated values are not far off from it (e.g. Norfolk et al., 2021). Very small grains will be removed from the system due to the effect of radiation pressure (or stellar winds around low-mass stars). The critical size is called the blow-out size and corresponds to a size for which the ratio between the radiation and gravitational force is $1/2$. Smaller grains are put on hyperbolic orbits once released from larger bodies on nearly circular orbits exiting the system on very short timescales. Assuming perfect blackbody grains, the blow-out size can be written as

$$D_{\text{bl}} = 0.8 \left(\frac{L_{\star}}{L_{\odot}} \right) \left(\frac{M_{\star}}{M_{\odot}} \right)^{-1} \left(\frac{\rho}{2.7 \text{ g cm}^{-3}} \right) \mu\text{m}, \quad (2)$$

where ρ is the density of solids. Now, given a minimum size D_{bl} , maximum size D_{\max} and $q = 11/6$, the total solid mass in a disc is given by

$$M_{\text{tot}} = 85 \left(\frac{f_{\text{IR}}}{10^{-3}} \right) \left(\frac{r}{100 \text{ au}} \right)^2 \left(\frac{D_{\max}}{10 \text{ km}} \right)^{0.5} \left(\frac{D_{\text{bl}}}{1 \mu\text{m}} \right)^{0.5} M_{\oplus}. \quad (3)$$

The total disc mass will be a function of time as planetesimals grind down and small dust is ejected from the system. Generally speaking we have that $dM_{\text{tot}}/dt = -M_{\text{tot}}/t_c$, where t_c is the collisional timescale of the largest planetesimal. We can estimate the collisional timescale if we further assume the solids strength or disruption threshold is independent of size, $q = 11/6$, the dispersion of eccentricities and inclinations are equal, and that the smallest body able to fragment the largest planetesimals is much smaller than D_{\max} . Under these assumptions the collisional timescale of

the largest planetesimal becomes (Wyatt et al., 2007b)

$$t_c = 450 \left(\frac{r}{100 \text{ au}} \right)^{13/3} \left(\frac{dr}{r} \right) \left(\frac{D_{\max}}{10 \text{ km}} \right) \left(\frac{Q_D^*}{330 \text{ J kg}^{-1}} \right)^{5/6} \left(\frac{e}{0.1} \right)^{-5/3} \left(\frac{M_\star}{M_\odot} \right)^{-4/3} \left(\frac{M_{\text{tot}}}{85 M_\oplus} \right)^{-1} \text{ Myr}, \quad (4)$$

where dr is the width of the disc, Q_D^* is the disruption threshold of planetesimals. Since t_c is inversely proportional to M_{tot} , the disc mass will evolve as $M_{\text{tot}}(t) = M_{\text{tot}}(0)/(1 + t/t_c(0))$, where $M_{\text{tot}}(0)$ and $t_c(0)$ are the initial disc mass and collisional timescale. For $t \gg t_c(0)$, the largest planetesimals in a disc are in collisional equilibrium and the disc mass and fractional luminosity will decay as $1/t$. Note that $t = 0$ here represents the time at which the disc is stirred, which could be different from the age of the system. Regardless of the initial disc mass, $M_{\text{tot}} < M_{\text{tot}}(0)t_c(0)/t$, i.e. the maximum disc mass as a function of time is

$$M_{\text{tot}}^{\max} = 85 \left(\frac{r}{100 \text{ au}} \right)^{13/3} \left(\frac{dr}{r} \right) \left(\frac{D_{\max}}{10 \text{ km}} \right) \left(\frac{Q_D^*}{330 \text{ J kg}^{-1}} \right)^{5/6} \left(\frac{e}{0.1} \right)^{-5/3} \left(\frac{M_\star}{M_\odot} \right)^{-4/3} \left(\frac{t}{450 \text{ Myr}} \right)^{-1} M_\oplus. \quad (5)$$

Similarly, we can define a maximum fractional luminosity making use of Equation 3 and 5. We find

$$f_{\text{IR}}^{\max} = 10^{-3} \left(\frac{r}{100 \text{ au}} \right)^{7/3} \left(\frac{dr}{r} \right) \left(\frac{D_{\max}}{10 \text{ km}} \right)^{0.5} \left(\frac{D_{\min}}{1 \mu\text{m}} \right)^{-0.5} \left(\frac{Q_D^*}{330 \text{ J kg}^{-1}} \right)^{5/6} \left(\frac{e}{0.1} \right)^{-5/3} \left(\frac{M_\star}{M_\odot} \right)^{-4/3} \left(\frac{t}{450 \text{ Myr}} \right)^{-1}. \quad (6)$$

The equations above provide very useful and simple ways of estimating collisional lifetimes and evolution of discs, which in contrast to more realistic numerical simulations they allow to quickly compute the evolution of thousands of models. This is particularly useful for population synthesis models. Based on these equations and infrared surveys, Wyatt et al. (2007a) and Sibthorpe et al. (2018) showed how population synthesis models can constrain the average values of $M_{\text{tot}}(0)$, D_{\max} , Q_D^* and e , which determine the initial fractional luminosity of discs and their collisional lifetime. Equation 6 also predicts that a disc older than t_c , will have a surface density that scales with radius as $r^{7/3}$, independently of the initial surface density (Kennedy & Wyatt, 2010). Thus by constraining the slope of the surface

density distribution of a disc, it is possible to test if $t_c(0)$ is shorter or longer than the age of the system or stirring timescale (Marino et al., 2017a,b). Moreover, a disc inner edge that is sharper than $r^{7/3}$ might indicate that the disc inner edge was truncated by a planet (e.g. Marino et al., 2018a, 2019; Matrà et al., 2020; Marino, 2021). For a recent and detailed discussion on the collisional evolution of debris discs and their inferred masses, see Krivov & Wyatt (2021).

3.1. *The outliers*

While the model presented above can account for the majority of discs, two types of discs remain hard to explain with standard collisional models.

First, 10-30% of nearby stars present emission in the near- or mid-IR that indicates the presence of high levels of hot or warm dust (Kral et al., 2017; Ertel et al., 2020; Absil et al., 2021). The warm dust is typically located at distances of ~ 1 au, i.e. analogous to the Zodiacal cloud in the Solar System and thus often referred as *exozodis*. While in principle, dust can be produced at any distance from the star if there are planetesimals colliding, in many systems the fractional luminosities of the hot and warm dust are orders of magnitude above the maximum levels expected for their ages and inferred dust radii (Wyatt et al., 2007b). This means that the dust is likely produced by an alternative mechanism. In the case of the hot dust, it is located near the sublimation radius and dominated by small grains (Kirchschlager et al., 2017). Whilst it is expected that dust produced in an exterior planetesimal belt will migrate inwards through P-R drag and reach the inner regions (in the absence of very massive planets, Bonsor et al., 2018), this dust does not remain for long enough in the inner regions to explain the near-IR excesses (van Lieshout et al., 2014; Sezestre et al., 2019). Pearce et al. (2020) recently showed that the gas originating from the sublimation of dust could push dust outwards, counterbalance the effect of P-R drag, and thus explain the pile-up of dust near the sublimation radius. Two main ideas have been proposed to explain the origin of the warm dust. For a large fraction of systems, P-R drag would be efficient enough to explain the observed mid-IR levels (Kennedy et al., 2015; Rigley & Wyatt, 2020). However, the warm dust in some systems needs to be resupplied faster, which could be achieved via exocomets being transported in via scattering or resonances (Bonsor & Wyatt, 2012; Bonsor et al., 2012, 2013, 2014; Marboeuf et al., 2016; Faramaz et al., 2017; Marino et al., 2018b).

Finally, the warm dust in some systems could be a transient phenomena

such as the product of a recent giant collisions (Jackson & Wyatt, 2012; Genda et al., 2015; Watt et al., 2021), which are expected in the last stages of terrestrial planet formation (Chambers, 2013). This is especially favoured in systems with fractional luminosities above 1%, which are termed *extreme debris discs* (EDDs Balog et al., 2009), and systems displaying mid-IR spectroscopic features that indicate the presence of very small crystalline dust particles (Rhee et al., 2008; Lisse et al., 2009; Olofsson et al., 2012). Some systems even display variability in their mid-IR emission as expected in a giant collision scenario (Meng et al., 2014, 2015; Su et al., 2019; Moór et al., 2021; Rieke et al., 2021), or even have short-lived gas (Marino et al., 2017a; Schneiderman et al., 2021).

4. Resolved observations

Whilst unresolved observations provide information about some of the most fundamental properties of debris discs, it is only through resolved observations that we can access their detailed structure. Given the wide size distribution of dust and the grain size dependence on the opacity, observations at different wavelength trace different ranges of grain sizes.

4.1. Scattered light observations

Observations at short wavelengths are sensitive to smaller grains, whose distribution is highly affected by radiation pressure or stellar winds. Both effects can put grains smaller than the blow-out size on hyperbolic orbits and make slightly larger grains to spiral inwards towards the star (e.g. Thébault & Wu, 2008; Plavchan et al., 2005). This is why observations at these wavelengths usually display large halos beyond the planetesimal disc (e.g. out to 1000 au around β Pic, Janson et al., 2021). At optical and near-IR wavelengths, the combination of negligible cold dust thermal emission (see Figure 1) and high stellar fluxes means that the disc flux is dominated by stellar light that is scattered by small dust. These observations are thus often called scattered light observations. In the last three decades, dozens of scattered light images have been obtained from the ground and space (e.g. Esposito et al., 2020; Schneider et al., 2014).

Several important properties can be derived from scattered light observations that relate to the intrinsic structure and composition of dust grains. First, by measuring the disc scattered light flux ($F_{\text{scat},\lambda}$), fractional luminosity, and stellar flux ($F_{\star,\lambda}$), a first order estimate of the albedo can

be obtained as $F_{\text{scat},\lambda}/(F_{\text{scat},\lambda} + f_{\text{IR}}F_{\star,\lambda})$ (Marshall et al., 2018). These estimates, however, typically assume isotropic scattering, while in reality scattering is anisotropic, making discs brighter towards their near side (i.e. light is preferentially scattered forward, e.g. Kalas et al., 2005). A more robust approach is to characterize how the surface brightness varies as a function of scattering angle, i.e. the scattering phase function. Observations of a disc inclined by i relative to a pole on orientation cover a range of scattering angles from $(90^\circ - i)$ to $(90^\circ + i)$. Therefore, highly inclined discs are ideal to sample this phase function over a wide range of scattering angles (e.g. Milli et al., 2017). In addition, polarized scattered light observations can be used to constrain the degree of polarization (Perrin et al., 2015). Scattered light emission can also be characterised as a function of wavelength adding more constraints to the size distribution and composition of grains, although strong degeneracies still remain (Köhler et al., 2008).

These properties have been characterised for multiple systems finding some similarities. For example, their phase functions are very similar showing a strong forward scattering peak, a moderate backward scattering peak, and a flat phase function at intermediate scattering angles (Hughes et al., 2018), which are consistent with porous grains with properties similar to Zodiacal and cometary dust (Graham et al., 2007; Ahmic et al., 2009). Polarised observations of HR 4796 also suggests grains are porous (Milli et al., 2019), although some studies have found compact grains are preferred when scattered light and thermal emission observations are fitted simultaneously (Rodigas et al., 2015; Ballering et al., 2016). On the other hand, albedo estimates typically range between 0.06-0.6 and typically exclude pure water ice compositions (Schneider et al., 2006; Choquet et al., 2018; Marshall et al., 2018; Romero et al., 2021). This range of albedos in addition to small, but yet significant, differences in the phase function of discs suggests a diversity in the properties of small dust in debris discs. In order to improve these constraints, it is necessary to move towards comprehensive models that can reproduce multiwavelength observations, taking into account the dynamics and spatial segregation of different grains sizes as well as their optical properties (e.g. Pawellek et al., 2019).

4.2. *Thermal emission at mm wavelengths*

At longer wavelength, the emission is dominated by thermal radiation. In what follows I will focus on mm ALMA observations. Since the dust opacity

decreases steeply at wavelengths longer than the grain size, mm observations are dominated by $\sim 0.1 - 10$ mm-sized grains, which are not affected by radiation pressure. Therefore, their distribution traces the distribution of their parent planetesimals. Figure 2 shows a gallery of exoKuiper belts imaged with ALMA, displaying a diversity of morphologies from narrow (bottom) to wide belts (middle), some split by gaps (top left and middle), and one eccentric belt that is offset from the star (bottom right).

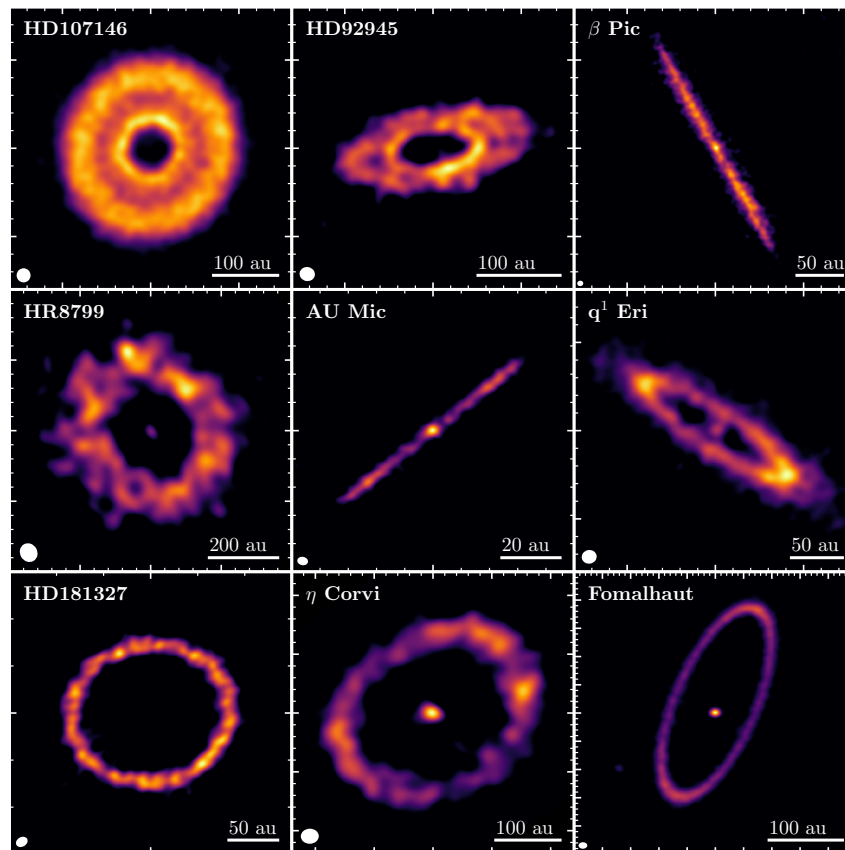


Fig. 2. ALMA clean images of 9 exoKuiper belts (Marino et al., 2018a, 2019; Matrà et al., 2019a; Faramaz et al., 2021; Daley et al., 2019; Lovell et al., 2021b; Pawellek et al., 2021; Marino et al., 2017a; MacGregor et al., 2017). The white ellipses at the bottom left show the beam size, while the white line at the bottom right provides a scale in au. The big and small ticks along the edges are separated by $5''$ and $1''$, respectively.

In the following subsections, I provide an overview of the main features that have been observed in exoKuiper belts using ALMA dust continuum observations. I start by describing some general trends and characteristics, such as the radius and width of exoKuiper belts (§4.2.1 and §4.2.2), and then discuss more detailed substructures that have been found, some of which are displayed in Figure 2.

4.2.1. *Radius distribution*

One of the most general and first goals of ALMA for debris discs studies was to resolve a large sample of exoKuiper belts and measure their radii. As described in §2, this cannot be accurately done by looking at SEDs and thus resolved observations are necessary. ALMA still is the best instrument to image exoKuiper belts thanks to its high sensitivity and adjustable resolution, which allows to tailor every observation depending on system properties such as its distance. During the first years of ALMA, big efforts were put on imaging every known belt with sufficient flux at mm wavelengths to be resolved. By 2018, we had resolved 26 exoKuiper belts around AFGKM stars, which Matrà et al. (2018) analysed to show that belts tend to be larger around more massive and luminous stars. This result was tested against observational biases that would make it hard to detect cold and large belts around less luminous stars, and collisional evolution which would quickly deplete small belts around more luminous stars. Those tests showed that both effects were unlikely to explain the trend, suggesting that this was a correlation present since exoKuiper belts are born. It is possible that this relation arises from planetesimal belts forming at preferred locations in protoplanetary disks (e.g. near the CO snow line), which scale with stellar properties, but this hypothesis has not been confirmed by models or further observations.

The radius luminosity relation motivated the REsolved ALMA and SMA Observations of Nearby Stars (REASONS) survey, which is the follow up of the JCMT SONS survey (Holland et al., 2017). The aim of REASONS was to double the sample size of millimeter-resolved debris discs, and model all discs (including archival observations) to derive their radius and width in a consistent manner. Preliminary results shown in Figure 3 (Sepulveda et al., 2019, Matrà et al. in prep.), including one additional observation of Fomalhaut C (Cronin-Coltsmann et al., 2021), indicate that the trend still holds in a sample of 52 systems.

The new preliminary results show a significantly larger dispersion, but

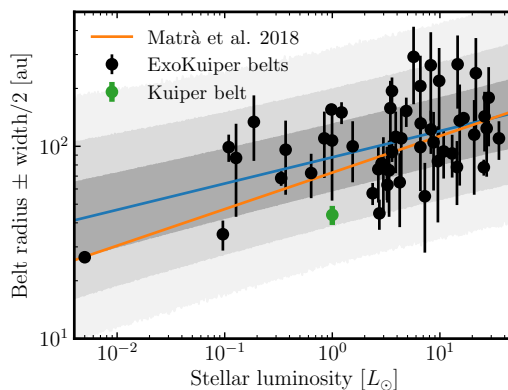


Fig. 3. ExoKuiper belts radii (black) vs stellar luminosity from the REASONS survey and Cronin-Coltman et al. (2021). The Kuiper belt is shown in green. The errorbars represent half of the full-width-half-maximum. The orange line shows the previous best fit in Matrà et al. (2018), while the blue line shows the new best fit. The grey shaded regions represent the 68%, 95% and 99.7% confidence regions taking into account a fit to the intrinsic dispersion (assumed to be constant across stellar luminosity).

the trend is still significant (blue line). Note that similar trends are known in protoplanetary discs, with discs around more massive stars being larger on average (Andrews et al., 2018). It is still an open question if these two relations are linked or if the location of exoKuiper belts is connected with the CO snow line location. Finally, it is worth noting as well that the Kuiper belt is small compared to the majority of belts around FGK stars, although the exoKuiper belts in this sample are much more massive than the Kuiper belt due to the sensitivity limit of current instruments. Smaller exoKuiper belts could be intrinsically less massive and fainter.

4.2.2. Widths

Together with the radius information, REASONS has also constrained the width of ~ 40 belts. The results show that most belts are relatively wide, with a median fractional width (the ratio between the width and radius) of 0.74. Figure 4 shows the distribution of fractional widths of exoKuiper belts (blue), revealing that there is not a typical width, but rather a wide distribution. Narrow belts like the one around Fomalhaut are rare. In fact, even the Kuiper belt seems to be much narrower than most belts.

Figure 4 also shows the fractional widths of dust rings in protoplanetary discs with radii between 30 to 250 au (orange). Those rings occupy the

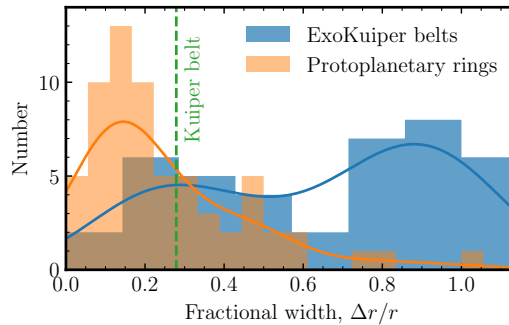


Fig. 4. Histogram of the fractional width of exoKuiper belts from the REASONS survey (blue, Matrá et al. in prep) and rings in protoplanetary discs (orange, Huang et al., 2018; Long et al., 2018; Cieza et al., 2021). The green dashed line represents the fractional width of the Kuiper belt estimated using the full-width-half-maximum of the L7 synthetic model of the inner, main and outer Kuiper belt (Kavelaars et al., 2009; Petit et al., 2011). The solid lines represent kernel density estimations using a Gaussian kernel.

same range of radii as exoKuiper belts, but are much narrower with a median fractional width of 0.18. This difference is interesting, since those dusty rings are ideal places for planetesimal formation (Stammler et al., 2019; Carrera et al., 2021), and thus we would expect exoKuiper belts to be similar or even narrower. Nevertheless, as recently shown by Miller et al. (2021), the large width of exoKuiper belts could be explained if those rings migrate forming planetesimals at a wide range of radii. Those rings would naturally migrate if, for example, they were caused by planets. In that case, the width of debris discs would imply migration rates higher than 5 au Myr^{-1} in order to cover distances of 50-100 au in the 5-10 Myr protoplanetary disc lifetimes.

4.2.3. Radial structures

In addition to measuring the central radius and widths, ALMA’s resolving power has uncovered the radial substructures in multiple wide exoKuiper belts. Figure 5 shows the surface density profiles of six belts, which display different features. For example, HD 107146, HD 92945, HD 206893 and possibly AU Mic show gaps (Marino et al., 2018a, 2019, 2020a; Nederlander et al., 2021; Daley et al., 2019) that could have been carved by planets orbiting within those gaps through scattering (Morrison & Malhotra, 2015). If those planets have not migrated, the width of those gaps (Δ_{gap}) should be roughly equal to the chaotic zone (Wisdom,

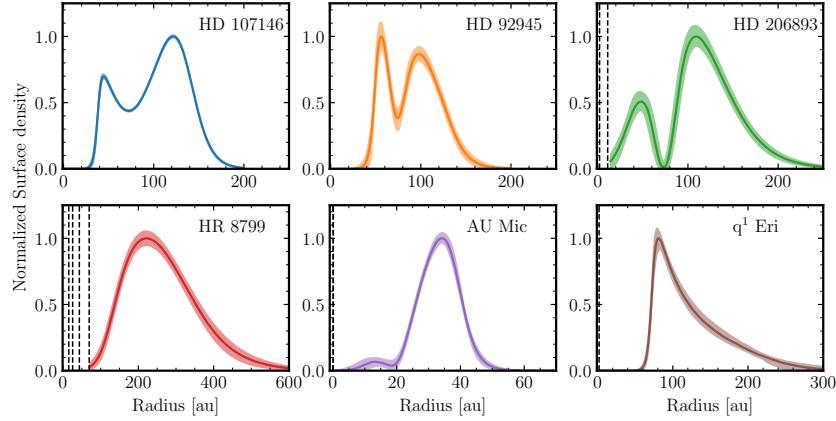


Fig. 5. Surface density radial profiles of 6 exoKuiper belts observed with ALMA. The profiles were retrieved using parametric models that were sensitive to the presence of gaps and the smoothness of the inner and outer edges (Marino, 2021). The shaded regions correspond to the 68% confidence interval. The vertical dashed lines show the location of known planets in these systems.

1980), i.e. $\Delta_{\text{gap}} \approx 3a_{\text{plt}}(M_{\text{plt}}/M_{\star})^{2/7}$, where a_{plt} , M_{plt} and M_{\star} are the planet semi-major axis, its mass, and the stellar mass, respectively. The gaps in HD 92945 and HD 206893 are centred at roughly 75 au and span $\sim 15 - 30$ au, which would suggest planet masses in between Neptune’s and Jupiter’s. HD 107146’s gap is very wide, but not deep enough to be explained by a single planet. It is also possible that the gaps were open by planets closer in through secular interactions (Pearce & Wyatt, 2015; Yelverton & Kennedy, 2018; Sefilian et al., 2021), in which case they would likely be asymmetric (which has only been excluded for HD 107146). Gaps have been also been found in scattered light observations tracing smaller grains (Golimowski et al., 2011; Schneider et al., 2014; Engler et al., 2019; Perrot et al., 2016; Bonnefoy et al., 2017; Feldt et al., 2017; Boccaletti et al., 2019; Ren et al., 2021). Gaps in the distribution of small grains could be generated by the photoelectric instability if gas is present (Lyra & Kuchner, 2013; Richert et al., 2018), which is the case in some of these discs (e.g. HD 141569 and HD 131835, see §5).

Another interesting feature is the inner and outer edges of the belts. As discussed in §3, sharp inner edges might indicate that discs were truncated by an interior planet. On the other hand, outer edges can be used to constrain the level of dynamical excitation of a disc as the higher the dis-

portion of eccentricities is, the smoother the edge will be (Marino, 2021). Among the 6 discs shown in Figure 5, HD 206803, HR 8799 and η Eri have the smoothest outer edges. The first two are known to host gas giant planets just interior to their discs (Marois et al., 2010; Milli et al., 2017), which could have scattered a large amount of solids onto eccentric orbits producing smooth outer edges, similar to the scattered component of the Kuiper belt. Scattered populations could explain as well the halos seen in ALMA observations of a few discs (Marino et al., 2016; MacGregor et al., 2018).

Finally, there are also some narrow belts that are known to be eccentric (e.g. Fomalhaut, HR 4796, HD 202628, HD 15115, HD 106906, Kalas et al., 2005; Rodigas et al., 2015; Krist et al., 2012; Sai et al., 2015; Kalas et al., 2015). This has normally been attributed to the presence of an eccentric planet inducing an eccentricity in the belt through secular interactions (Wyatt et al., 1999; Quillen, 2006; Chiang et al., 2009; Nesvold et al., 2013; Pearce & Wyatt, 2014). However, Kennedy (2020) recently showed that two of these discs (Fomalhaut and HD 202628) appear narrower than expected in that scenario, suggesting that either the belts were born eccentric or eccentricities are damped leading to narrower belts.

4.2.4. Vertical structures

The vertical structure of exoKuiper belts can also provide key information about the dynamics of these systems. Studies of near to edge-on belts are ideally suited for this. The best example is perhaps β Pic, which has a large and bright edge-on disc. HST and ground-based scattered light images of this disc showed that it is warped (Mouillet et al., 1997; Heap et al., 2000; Golimowski et al., 2006), which was attributed to an inner companion misaligned to the disc midplane (Mouillet et al., 1997; Augereau et al., 2001). This putative planet was later discovered through direct imaging (Lagrange et al., 2009), in rough agreement with the misaligned scenario (Dawson et al., 2011; Nesvold & Kuchner, 2015).

Furthermore, the vertical distribution of the disc is significantly deviated from a simple Gaussian distribution (Golimowski et al., 2006; Matrà et al., 2019a). In a disc of interacting planetesimals, the distribution of inclinations is expected to follow a Rayleigh distribution (Ida & Makino, 1992), which translates to a Gaussian particle density distribution. However, β Pic's disc is better described by two Gaussians. Matrà et al. (2019a) argued that the population with high inclinations could result as a con-

sequence of an additional planet migrating out. This scenario would be similar to Neptune's outward migration that led to the two dynamical populations in the classical Kuiper belts (Brown, 2001; Nesvorný, 2015).

AU Mic is another well known system with an edge-on disc around an M star. Using ALMA, Daley et al. (2019) showed that the disc height is consistent with an inclination dispersion of $\sim 3^\circ$ and that such an excitation could be produced by planetesimals larger than 400 km embedded in the disc. This disc also shows fast outward moving clumps in scattered light, some of which seem to be unbound (Boccaletti et al., 2018). These clumps would be made of small grains that are on unbound trajectories due to strong stellar winds by this young M star. However, what creates the clumps is still highly uncertain. Proposed scenarios range from a compact body embedded in the belt releasing dust (Sezestre et al., 2017), a collisional avalanche at the intersection of two belts (Chiang & Fung, 2017), or asymmetric disc winds (Wisniewski et al., 2019).

5. Circumstellar gas

While debris discs are generally considered gas poor, it has been known for more than two decades that some debris disc systems have gas that is readily detectable as absorption lines in the UV and optical, or as emission lines at far-IR and mm wavelengths (Slettebak, 1975; Zuckerman et al., 1995). Historically, these two types of observations have been studied as independent phenomena, although several systems present both. Below, I summarise the main characteristics of these lines and their potential origins and implications.

5.1. Absorption lines

The first known and best studied system with circumstellar absorption lines is β Pic. Slettebak (1975) found narrow CaII H&K absorption lines in the stellar spectrum. Subsequent studies found that these and FeII lines in the UV change with time (Kondo & Bruhweiler, 1985; Lagrange et al., 1987). Ferlet et al. (1987) showed how these absorption lines can be decomposed into stable narrow lines at the stellar velocity and Doppler shifted lines that vary in timescales of months, days and hours. These variations were attributed to the presence of star-grazer objects or *falling evaporating bodies* on highly eccentric orbits that sublimate within a few stellar radii producing the observed warm gas (Beust et al., 1990; Kiefer et al., 2014). More

recently, Kennedy et al. (2018) showed how individual absorption features accelerate over several hours, and this acceleration constrains the orbits of these *exocomets*. Today we know that this phenomenon is common, and more likely to be detected in systems with debris discs that are edge-on (e.g. Welsh et al., 1998; Eiroa et al., 2016; Hales et al., 2017; Iglesias et al., 2018; Rebollido et al., 2020). For a more in depth description of the gas seen in absorption and its comparison with Solar System comets see the recent review by Strøm et al. (2020).

5.2. Emission lines

Colder gas seen in emission at far-IR and mm wavelengths have also been found in debris discs. At first, this gas was mainly found around young A stars with bright debris discs (e.g. Zuckerman et al., 1995; Kóspál et al., 2013; Cataldi et al., 2014; Dent et al., 2014; Moór et al., 2017), but deeper observations, especially with ALMA, have shown that CO gas can also be found in older systems (Matrà et al., 2017), and later type stars (Marino et al., 2016, 2017a; Matrà et al., 2019b; Kral et al., 2020b).

The origin of this gas in many of these systems is still a subject of debate. Zuckerman & Song (2012) hypothesised that the CO gas could be released by the same planetesimals that resupply the dust if these were volatile rich (i.e. exocomets). As solids fragment due to collisions, CO gas that was trapped in pockets could be release, and thus debris discs should release exocometary gas as they collisionally evolve. The rate at which gas is released would be a fraction of the disc mass loss rate, and this fraction should be close to the abundance of volatiles in exocomets. However, Zuckerman & Song (2012) realised the gas release rate would not be enough to balance the rate at which CO was being destroyed. If unshielded, CO molecules quickly photodissociate due to stellar or interstellar UV photons in timescales of $\lesssim 100$ yr (Visser et al., 2009). This meant that this *secondary origin* scenario could explain the low CO levels in some systems and provide constraints on the abundance of CO in their exocomets (e.g. HD 181327, β Pic and Fomalhaut it was found to be consistent with Solar System comets, Marino et al., 2016; Kral et al., 2016; Matrà et al., 2017), but not the high CO levels around some young A stars. It was concluded that the CO gas in those stars was likely a leftover from their protoplanetary discs and shielded by leftover H₂ gas. These systems were tagged as hybrid, containing secondary dust and primordial gas (Kóspál et al., 2013).

This hybrid nature was recently challenged by Kral et al. (2019) that

proposed that the same carbon produced by the CO photodissociation could shield CO from the interstellar UV, increasing the CO lifetime by orders of magnitude. This longer lifetime due to carbon shielding would explain the high CO levels around young A stars and would only happen to those that are born with the most massive debris discs (Marino et al., 2020b), disfavoured FGK stars that tend to have lower mass discs. More recent observations have found abundant carbon gas in some of the systems with high CO levels that are expected to be shielded (Kral et al., 2019; Higuchi et al., 2019; Cataldi et al., 2020), although it is still an open question if the observed carbon levels are high enough. The gas evolution and shielding of CO gas are described below.

5.3. Evolution of exocometary gas

Once this gas is released from planetesimals it is expected to spread forming an accretion disc (Kral et al., 2016), unless radiation pressure or stellar winds are strong enough to blow out the gas (Youngblood et al., 2021; Kral et al., 2021). How massive such a gaseous circumstellar disc can be depends on the rate at which gas is being released and the rate at which gas is lost via accretion onto the central star or inner bodies. The accretion rate will depend on the efficiency of the angular momentum transport, either through a kinematic viscosity (e.g. if the magnetorotational instability is active) or disc winds (Kral & Latter, 2016). So far, models assume the disc is evolving viscously and parametrise the viscosity through the classical alpha disc model with $\nu = \alpha c_s^2 / \Omega_K$, where c_s , Ω_K and α are the sound speed, Keplerian frequency and a dimensionless free parameter smaller than one. A population synthesis study by Marino et al. (2020b) found a good agreement between models and observations with $\alpha \sim 0.1$, although its value still is very uncertain given the assumptions in these models. Below I describe how the gas is expected to viscously evolve.

Once gas is released in the form of CO, it will photodissociate into carbon and oxygen atoms. Since the CO lifetime is only about ~ 100 yr, it will stay co-located with the dust and planetesimals. Carbon and oxygen, on the other hand, will accumulate and viscously spread on longer timescales. This behaviour is shown in the top panels of Figure 6, which assume CO gas is released at a rate of $2 \times 10^{-4} M_{\oplus} \text{ Myr}^{-1}$ from a belt of planetesimals centred at 100 au and 50 au wide around a $10 L_{\odot}$ star, $\alpha = 10^{-2}$, and carbon is mostly neutral (only neutral carbon can shield CO). With these values, neutral carbon (CI) never reaches the critical surface density of

$10^{-7} M_{\oplus} \text{ au}^{-2}$ (grey dashed line) and thus it is ineffective at shielding CO. This is why the CO surface density stays roughly constant over 100 Myr and does not spread beyond the belt. If the gas release rate is higher, e.g. $2 \times 10^{-2} M_{\oplus} \text{ Myr}^{-1}$ (as shown in bottom panels of Figure 6), CI reaches the critical surface density, after which CO becomes shielded and viscously spreads to the inner and outer regions. These simulations were done with the python package EXOGAS^a that is based on the software developed in Marino et al. (2020b), with the addition of photon counting to correctly calculate the photodissociation timescale of CO (Cataldi et al., 2020).

Note that these simulations assume that most of carbon sits in an upper layer on top of the CO gas, however, if they are well mixed shielding by carbon becomes much less effective (Cataldi et al., 2020). Therefore, observations that can constrain the vertical distribution of CO and carbon gas are required to assess how effective carbon is at shielding CO. Finally, although these simulations assume a constant CO release rate, this is expected to decrease with time, which means the gas levels can be out of

^aEXOGAS can be downloaded from <https://github.com/SebaMarino/exogas>. If you would like to use it in a publication, please get in touch.

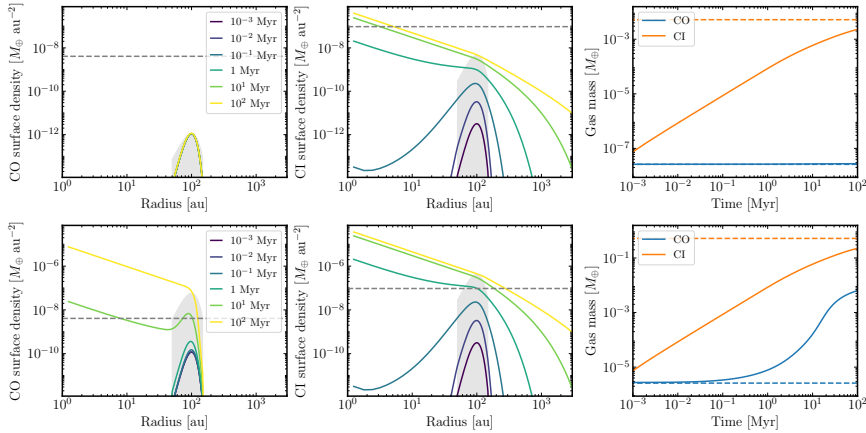


Fig. 6. Evolution of circumstellar CO and CI gas as it is released from a debris disc at 100 au according to the python package EXOGAS (Marino et al., 2020b). The left and middle panels show the surface density of CO and CI at different epochs, respectively. The right panels show the evolution of the total CO and CI mass. The grey dashed lines represent the surface density at which the CO and CI become optically thick to photodissociating UV photons in the vertical direction. The blue and orange dashed lines show the expected mass in steady-state if CO is unshielded.

equilibrium and quickly evolving from a shielded onto an unshielded state (Marino et al., 2020b).

5.4. Implications

Understanding the evolution of this exocometary gas is important for several reasons. First, the chemical composition of this gas encodes the composition of planetesimals. Therefore, by understanding how this gas evolves it would be possible to constrain the volatile composition of exocomets, even in shielded discs. Second, as it viscously spreads, the gas could be accreted by gas giant planets in the inner regions and potentially change their abundances of volatile elements in their atmosphere (Marino et al., 2020b). This would make even more difficult to trace the formation location of gas giants based on their atmospheric abundances (Öberg et al., 2011). Finally, the exocometary gas could also be accreted by low mass planets in the habitable zone, building new secondary atmospheres with exocometary composition over tens of Myr’s (Kral et al., 2020a).

Acknowledgements: I would like to thank the organisers of the Severo-Ochoa advanced school “Planets, exoplanets and their systems in a broad and multidisciplinary context”, which this review chapter is based on. I would also like to thank Grant Kennedy, Luca Matrà and Josh Lovell for providing ALMA images of Fomalhaut, β Pic and η Eri.

References

- Absil, O; et al., 2021. *A&A*, 651:A45.
Ahmic, M; et al., 2009. *ApJ*, 705:529.
Andrews, SM; et al., 2018. *ApJ*, 865:157.
Augereau, JC; et al., 2001. *A&A*, 370:447.
Aumann, HH; et al., 1984. *ApJ*, 278:L23.
Backman, D; et al., 2009. *ApJ*, 690:1522.
Backman, DE et al., 1993. In EH Levy & JI Lunine, eds., *Protostars and Planets III*. 1253–1304.
Ballerig, NP; et al., 2014. *ApJ*, 793:57.
Ballerig, NP; et al., 2016. *ApJ*, 823:108.
Balog, Z; et al., 2009. *ApJ*, 698:1989.
Beust, H; et al., 1990. *A&A*, 236:202.
Blum, J et al., 2008. *Annual Review of Astronomy and Astrophysics*, 46:21.
Boccaletti, A; et al., 2018. *A&A*, 614:A52.
Boccaletti, A; et al., 2019. *A&A*, 625:A21.
Bonnefoy, M; et al., 2017. *A&A*, 597:L7.
Bonsor, A; et al., 2012. *A&A*, 548:A104.

- Bonsor, A et al., 2012. MNRAS, 420:2990.
Bonsor, A; et al., 2013. MNRAS, 433:2938.
Bonsor, A; et al., 2014. MNRAS, 441:2380.
Bonsor, A; et al., 2018. MNRAS, 480:5560.
Booth, M; et al., 2013. MNRAS, 428:1263.
Brown, ME, 2001. AJ, 121:2804.
Carrera, D; et al., 2021. AJ, 161:96.
Casassus, S; et al., 2019. MNRAS, 483:3278.
Cataldi, G; et al., 2014. A&A, 563:A66.
Cataldi, G; et al., 2020. ApJ, 892:99.
Chambers, JE, 2013. Icarus, 224:43.
Chen, CH; et al., 2009. ApJ, 701:1367.
Chiang, E; et al., 2009. ApJ, 693:734.
Chiang, E et al., 2017. ApJ, 848:4.
Choquet, É; et al., 2018. ApJ, 854:53.
Cieza, LA; et al., 2021. MNRAS, 501:2934.
Cronin-Coltsmann, PF; et al., 2021. MNRAS, 504:4497.
Daley, C; et al., 2019. ApJ, 875:87.
Dawson, RI; et al., 2011. ApJ, 743:L17.
Dent, WRF; et al., 2014. Science, 343:1490.
Dohnanyi, JS, 1969. J. Geophys. Res., 74:2531.
Dominik, C et al., 2003. ApJ, 598:626.
Dullemond, CP; et al., 2018. ApJ, 869:L46.
Eiroa, C; et al., 2013. A&A, 555:A11.
Eiroa, C; et al., 2016. A&A, 594:L1.
Engler, N; et al., 2019. A&A, 622:A192.
Ertel, S; et al., 2020. AJ, 159:177.
Esposito, TM; et al., 2020. AJ, 160:24.
Faramaz, V; et al., 2017. MNRAS, 465:2352.
Faramaz, V; et al., 2021. AJ, 161:271.
Feldt, M; et al., 2017. A&A, 601:A7.
Ferlet, R; et al., 1987. A&A, 185:267.
Gáspár, A; et al., 2012. ApJ, 754:74.
Genda, H; et al., 2015. ApJ, 810:136.
Golimowski, DA; et al., 2006. AJ, 131:3109.
Golimowski, DA; et al., 2011. AJ, 142:30.
Graham, JR; et al., 2007. ApJ, 654:595.
Hales, AS; et al., 2017. MNRAS, 466:3582.
Heap, SR; et al., 2000. ApJ, 539:435.
Higuchi, AE; et al., 2019. ApJ, 883:180.
Holland, WS; et al., 2017. MNRAS, 470:3606.
Huang, J; et al., 2018. ApJ, 869:L42.
Hughes, AM; et al., 2018. ARA&A, 56:541.
Ida, S et al., 1992. Icarus, 96:107.
Iglesias, D; et al., 2018. MNRAS, 480:488.
Jackson, AP et al., 2012. MNRAS, 425:657.

- Janson, M; et al., 2021. *A&A*, 646:A132.
Johansen, A; et al., 2007. *Nature*, 448:1022.
Kalas, P; et al., 2005. *Nature*, 435:1067.
Kalas, PG; et al., 2015. *ApJ*, 814:32.
Kataoka, A; et al., 2013. *A&A*, 557:L4.
Kavelaars, JJ; et al., 2009. *AJ*, 137:4917.
Kennedy, GM, 2020. *Royal Society Open Science*, 7:200063.
Kennedy, GM et al., 2010. *MNRAS*, 405:1253.
Kennedy, GM et al., 2014. *MNRAS*, 444:3164.
Kennedy, GM; et al., 2015. *ApJS*, 216:23.
Kennedy, GM; et al., 2018. *MNRAS*, 475:4924.
Kenyon, SJ et al., 2008. *ApJS*, 179:451-483.
Kiefer, F; et al., 2014. *Nature*, 514:462.
Kirchschlager, F; et al., 2017. *MNRAS*, 467:1614.
Köhler, M; et al., 2008. *ApJ*, 686:L95.
Kondo, Y et al., 1985. *ApJ*, 291:L1.
Kóspál, Á; et al., 2013. *ApJ*, 776:77.
Kral, Q; et al., 2016. *MNRAS*, 461:845.
Kral, Q et al., 2016. *MNRAS*, 461:1614.
Kral, Q; et al., 2017. *The Astronomical Review*, 13:69.
Kral, Q; et al., 2019. *MNRAS*, 489:3670.
Kral, Q; et al., 2020a. *Nature Astronomy*, 4:769.
Kral, Q; et al., 2020b. *MNRAS*, 497:2811.
Kral, Q; et al., 2021. *A&A*, 653:L11.
Krist, JE; et al., 2012. *AJ*, 144:45.
Krivov, AV, 2010. *Research in Astronomy and Astrophysics*, 10:383.
Krivov, AV; et al., 2006. *A&A*, 455:509.
Krivov, AV et al., 2018. *MNRAS*, 479:3300.
Krivov, AV et al., 2021. *MNRAS*, 500:718.
Lagrange, AM; et al., 1987. *A&A*, 173:289.
Lagrange, AM; et al., 2009. *A&A*, 495:335.
Li, R et al., 2021. *ApJ*, 919:107.
Lisse, CM; et al., 2009. *ApJ*, 701:2019.
Löhne, T, 2020. *A&A*, 641:A75.
Löhne, T; et al., 2008. *ApJ*, 673:1123-1137.
Long, F; et al., 2018. *ApJ*, 869:17.
Lovell, JB; et al., 2021a. *MNRAS*, 500:4878.
Lovell, JB; et al., 2021b. *MNRAS*, 506:1978.
Luppe, P; et al., 2020. *MNRAS*, 499:3932.
Lyra, W et al., 2013. *Nature*, 499:184.
MacGregor, MA; et al., 2016. *ApJ*, 823:79.
MacGregor, MA; et al., 2017. *ApJ*, 842:8.
MacGregor, MA; et al., 2018. *ApJ*, 869:75.
Marboeuf, U; et al., 2016. *Planet. Space Sci.*, 133:47.
Marino, S, 2021. *MNRAS*, 503:5100.
Marino, S; et al., 2016. *MNRAS*, 460:2933.

- Marino, S; et al., 2017a. MNRAS, 465:2595.
Marino, S; et al., 2017b. MNRAS, 469:3518.
Marino, S; et al., 2018a. MNRAS, 479:5423.
Marino, S; et al., 2018b. MNRAS, 479:1651.
Marino, S; et al., 2019. MNRAS, 484:1257.
Marino, S; et al., 2020a. MNRAS, 498:1319.
Marino, S; et al., 2020b. MNRAS, 492:4409.
Marois, C; et al., 2010. Nature, 468:1080.
Marshall, JP; et al., 2018. ApJ, 869:10.
Matrà, L; et al., 2017. ApJ, 842:9.
Matrà, L; et al., 2018. ApJ, 859:72.
Matrà, L; et al., 2019a. AJ, 157:135.
Matrà, L; et al., 2019b. AJ, 157:117.
Matrà, L; et al., 2020. ApJ, 898:146.
Matthews, BC; et al., 2014. Protostars and Planets VI:521.
Meng, HYA; et al., 2014. Science, 345:1032.
Meng, HYA; et al., 2015. ApJ, 805:77.
Meshkat, T; et al., 2017. AJ, 154:245.
Michel, A; et al., 2021. arXiv e-prints:arXiv:2104.05894.
Miller, E; et al., 2021. MNRAS.
Milli, J; et al., 2017. A&A, 599:A108.
Milli, J; et al., 2019. A&A, 626:A54.
Moór, A; et al., 2017. ApJ, 849:123.
Moór, A; et al., 2021. ApJ, 910:27.
Morales, FY; et al., 2009. ApJ, 699:1067.
Morrison, S et al., 2015. ApJ, 799:41.
Mouillet, D; et al., 1997. MNRAS, 292:896.
Mustill, AJ et al., 2009. MNRAS, 399:1403.
Nederlander, A; et al., 2021. ApJ, 917:5.
Nesvold, ER; et al., 2013. ApJ, 777:144.
Nesvold, ER et al., 2015. ApJ, 815:61.
Nesvorný, D, 2015. AJ, 150:73.
Norfolk, BJ; et al., 2021. MNRAS.
Öberg, KI; et al., 2011. ApJ, 743:L16.
Olofsson, J; et al., 2012. A&A, 542:A90.
Pawellek, N; et al., 2014. ApJ, 792:65.
Pawellek, N; et al., 2019. MNRAS, 488:3507.
Pawellek, N; et al., 2021. MNRAS.
Pearce, TD et al., 2014. MNRAS, 443:2541.
Pearce, TD et al., 2015. MNRAS, 453:3329.
Pearce, TD; et al., 2020. MNRAS, 498:2798.
Perrin, MD; et al., 2015. ApJ, 799:182.
Perrot, C; et al., 2016. A&A, 590:L7.
Petit, JM; et al., 2011. AJ, 142:131.
Plavchan, P; et al., 2005. ApJ, 631:1161.
Quillen, AC, 2006. MNRAS, 372:L14.

- Rebollido, I; et al., 2020. *A&A*, 639:A11.
Ren, B; et al., 2021. *ApJ*, 914:95.
Rhee, JH; et al., 2008. *ApJ*, 675:777-783.
Ricci, L; et al., 2015. *ApJ*, 798:124.
Richert, AJW; et al., 2018. *ApJ*, 856:41.
Rieke, GH; et al., 2021. *ApJ*, 918:71.
Rigley, JK et al., 2020. *MNRAS*, 497:1143.
Rodigas, TJ; et al., 2015. *ApJ*, 798:96.
Romero, C; et al., 2021. *A&A*, 651:A34.
Rosotti, GP; et al., 2020. *MNRAS*, 495:173.
Sai, S; et al., 2015. *PASJ*, 67:20.
Schneider, G; et al., 2006. *ApJ*, 650:414.
Schneider, G; et al., 2014. *AJ*, 148:59.
Schneiderman, T; et al., 2021. *Nature*, 598:425.
Sefilian, AA; et al., 2021. *ApJ*, 910:13.
Sepulveda, AG; et al., 2019. *ApJ*, 881:84.
Sezestre, É; et al., 2017. *A&A*, 607:A65.
Sezestre, É; et al., 2019. *A&A*, 626:A2.
Sibthorpe, B; et al., 2018. *MNRAS*, 475:3046.
Slettebak, A, 1975. *ApJ*, 197:137.
Stammler, SM; et al., 2019. *ApJ*, 884:L5.
Strøm, PA; et al., 2020. *PASP*, 132:101001.
Su, KYL; et al., 2006. *ApJ*, 653:675.
Su, KYL; et al., 2019. *AJ*, 157:202.
Thébault, P et al., 2007. *A&A*, 472:169.
Thébault, P et al., 2008. *A&A*, 481:713.
van Lieshout, R; et al., 2014. *A&A*, 571:A51.
Veras, D, 2021. arXiv e-prints:arXiv:2106.06550.
Visser, R; et al., 2009. *A&A*, 503:323.
Watt, L; et al., 2021. *MNRAS*, 502:2984.
Weidenschilling, SJ, 1977. *MNRAS*, 180:57.
Welsh, BY; et al., 1998. *A&A*, 338:674.
Whipple, FL, 1973. *NASA Special Publication*, 319:355.
Wisdom, J, 1980. *AJ*, 85:1122.
Wisniewski, JP; et al., 2019. *ApJ*, 883:L8.
Wyatt, MC, 2008. *ARA&A*, 46:339.
Wyatt, MC; et al., 1999. *ApJ*, 527:918.
Wyatt, MC; et al., 2007a. *ApJ*, 663:365.
Wyatt, MC; et al., 2007b. *ApJ*, 658:569.
Yelverton, B et al., 2018. *MNRAS*, 479:2673.
Yelverton, B; et al., 2019. *MNRAS*, 488:3588.
Yelverton, B; et al., 2020. *MNRAS*, 495:1943.
Youdin, AN et al., 2005. *ApJ*, 620:459.
Youngblood, A; et al., 2021. arXiv e-prints:arXiv:2108.11965.
Zsom, A; et al., 2010. *A&A*, 513:A57.
Zuckerman, B; et al., 1995. *Nature*, 373:494.

Zuckerman, B et al., 2012. ApJ, 758:77.